


Coemergence of Dirac and multi-Weyl topological excitations in pnictide antiperovskites

Wen Fong Goh and Warren E. Pickett

Department of Physics, University of California, Davis, California 95616, USA (Received 8 May 2018; revised manuscript received 7 September 2018; published 28 September 2018)

The relatively unexplored family of pnictide-based antiperovskites has been shown to harbor prospects for topological phases. Using the example of Ca_3BiP , we demonstrate a cascade of phases as the initial cubic symmetry is broken successively. Initially a small-gap Z_2 topological insulator, spin-orbit coupling leads to band re-ordering resulting in a topological semimetal phase. Compressive uniaxial (001) strain leads back to a small-gap Z_2 topological insulator, with the expected gapless boundary modes. Tensile (001) strain leaves the system with a pair of Dirac points along $(0, 0, \pm k_z)$ pinning the Fermi level, producing an unusual double meniscus of connected Fermi arcs on the (100) and (010) surfaces. Finally, breaking time-reversal symmetry by an applied Zeeman field produces a new phase with a pair of multi-Weyl nodes (massive or massless depending on direction, conventionally called semi-Dirac in two-dimensional systems) simultaneous with a sister pair of Dirac modes along each $\pm k_z$ axis, combining to pin the Fermi level in the close vicinity of these varied single-particle excitations.

DOI: [10.1103/PhysRevB.98.125147](https://doi.org/10.1103/PhysRevB.98.125147)**I. INTRODUCTION**

Topological bulk phases have a valence-conduction band inversion that must become disentangled at an interface to vacuum (i.e., at a surface), giving rise to topologically protected gapless, conducting surface states [1]. In three dimensions (3D), a Z_2 topological insulator (TI) is characterized by a $Z_2 = 0$ or 1 topological invariant. Semimetals can also be classified by topological invariants, with the fourfold degenerate (including spin) Dirac point being the canonical example. Symmetry lowering has a strong impact. For a noncentrosymmetric [broken inversion symmetry (IS)] or magnetic [broken time reversal symmetry (TRS)] material, the effective low energy Hamiltonian for linear band crossing $\hbar v_F(\vec{\tau} \cdot \vec{k})$, where $\vec{\tau}$ are the Pauli matrices, has eigenvalues $E = \pm \hbar v_F |\vec{k}|$, with the sign providing the helicity of the Weyl particles [2]. There is an additional type of degeneracy: that of a conventional zero-gap semiconductor with quadratically touching bands that has no net topological character.

Intermediate between these degeneracies lie multi-Weyl points [3], from which dispersion proceeds as either *linear* (massless) or *quadratic* (massive) depending on direction. Multi-Weyl points are 3D generalizations of the semi-Dirac point in 2D that displays linear or quadratic dispersion depending on direction [4,5]. Such points reflect a universe in which the form of the kinetic energy operator depends on direction. These points are protected by symmetry; however, the semi-Dirac point in a broken TRS system can be driven by spin-orbit coupling to a Chern insulator phase [6].

To date several structural classes of topological materials have been discovered or predicted, beginning with the topological insulator (TI) $\text{Bi}_{1-x}\text{Sb}_x$ alloys [7], Bi_2Se_3 , and related families [8–12]. Other materials, viz., HgTe [13], α -Sn (gray tin), and halide perovskites [14], are not intrinsically topological but become so by tuning with strain to induce a topological phase. Likewise, families of topological semimetals (TSMs) have been predicted and pursued [15–19]. Surface probes such

as angle resolved photoemission spectroscopy (ARPES) and scanning tunneling microscopy (STM) are used to identify the corresponding topological surface states. In all of these systems, it is *sp* bands that provide the topological character.

The antiperovskite (APv) structure class of alkaline-earth and pnictides compounds has been proposed to harbor potential topological insulating phases [20,21]. Our density functional theory based survey of the entire class of $3 \times 5 \times 5$ possible alkaline-earth-pnictide APv compounds [21], viz., $\text{Ae}_3\text{Pn}_A\text{Pn}_B$, where $\text{Ae} = \text{Ca, Sr, Ba}$ and $\text{Pn}_A, \text{Pn}_B = \text{N, P, As, Sb, Bi}$, confirmed that some of these compounds in the assumed cubic structure host, or are very close to, nontrivial topological phases.

In this paper we choose a representative member of this proposed class and demonstrate that a sequence of symmetry lowering changes can propel a given compound through a cascade of phases that includes all of the above mentioned phases and into a class in which both Dirac and multi-Weyl excitations lie in the close vicinity of the Fermi level, thus determining the transport and low-energy bulk excitations and providing connected Fermi arcs in the boundary spectrum.

II. STRUCTURE, NOTATION, AND METHODS

This cubic APv structure (space group $Pm\bar{3}m$) has vertex-sharing Ae_6Pn_B octahedra, with Pn_A^{3+} ions in the interstitial *A* sites surrounded symmetrically by eight octahedra. Several nitrides in this class were surveyed by Niewa [22]. Our notation of elements *Ae*, Pn_A , and Pn_B follows that of an antiperovskite with general chemical formula X_3AB , where the *A* cation is 12-fold cubo-octahedral coordinated and *B* is sixfold coordinated by an octahedron of *X* cations. The central role of the anion was discussed previously; unlike in the oxide perovskites, the *A* site rather than the *B* site plays a central role in the electronic structure as it provides the uppermost

valence bands that border the gap or invert with the conduction bands.

To obtain the electronic structure of the APv compounds $Ae_3Pn_A Pn_B$, the all-electron density functional theory (DFT) full-potential local orbital (FPLO) method [23] was used with the generalized gradient approximation (GGA) exchange correlation of Perdew, Burke, and Ernzerhof (1996) [24]. A dense $20 \times 20 \times 20$ k -point mesh was used for self-consistency because of the delicate band overlap near Γ . Spin-orbit coupling (SOC) was included by using the fully relativistic four-component Kohn-Sham-Dirac equation implemented in FPLO, without resorting to the intermediate scalar relativistic approximation.

Analysis of the band topology was done by calculating the Z_2 topological invariants following the Fu-Kane prescription, based on parity eigenvalues at the time-reversal invariant momenta (TRIM) [25], which are available from the FPLO code. About a dozen compounds have nonzero Z_2 invariants in the assumed cubic structure [21]. The surface spectrum was obtained by first obtaining the maximally localized Wannier functions and corresponding hopping amplitudes [26,27]. A semi-infinite system is then constructed and the surface spectrum is calculated using the iterative surface Green's function method [28,29] with a tight-binding hopping cutoff of four unit cells.

III. DISCUSSION OF RESULTS

Our computational survey [21] established that of two given pnictides, the stable structure always has the largest of the pair occupying the A site. This anion provides the valence band maximum states; being the heaviest of the two pnictide atoms it provides the strongest SOC splitting, thus tending to promote inversion of valence and conduction bands and hence topological character. The lower conduction bands have $Ae d$ orbital character. The cubic aPV compounds are mostly narrow gap semiconductors, with both conduction band minimum and valence band maximum occurring at Γ , giving SOC a central role in band inversion.

When band inversion occurs, $Pn p$ orbitals with odd parity at Γ are shifted above the lowest a band which has even parity, due to p eigenvalue splitting by SOC. Figure 1 shows a rapid, almost abrupt shift in the s special character of Bi along X - Γ - Z . The threefold cubic degeneracy at the Γ point has to be connected by one conduction and two valence bands and results in a TSM state. By symmetry breaking, these TSMs can be transformed into TIs and Dirac semimetals.

A. Uniaxial compression

As a specific example, we consider Ca_3BiP , one of the narrow-gap APv semiconductors, as an example of a TI with Z_2 indices (1;000) before SOC is included. It has a calculated direct band gap of 0.16 eV at the Γ point and the p orbitals of the A site anion, Bi, lie at the bottom of the gap. SOC inverts the band ordering with an inversion energy of 0.28 eV, producing a topological band-touching semimetal due to degenerate $p_{3/2}$ states pinning the Fermi level. A compressive uniaxial strain in the range 1–7% (the range we have studied) breaks the crystal symmetry while maintaining the inverted

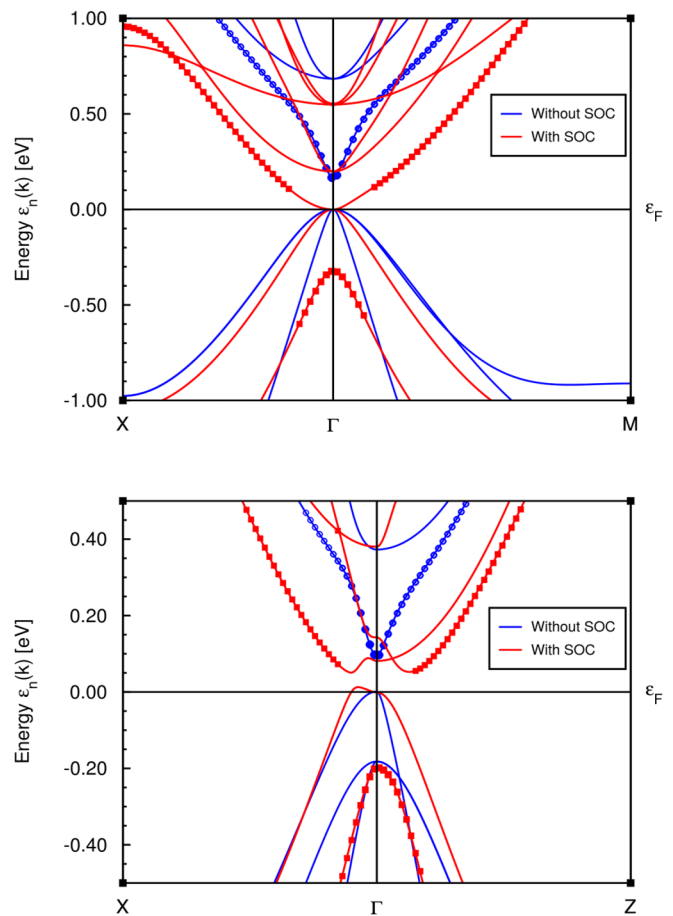


FIG. 1. Top panel: Without SOC (blue) cubic Ca_3BiP is a topological insulator with an anomalously small electron mass. SOC (red) reorders the bands, leaving a zero-gap semimetal. The large symbols denote Bi $6s$ character, demonstrating the sp band reordering with SOC. Bottom panel: 5% tetragonal compressive strain in Ca_3BiP results in a TI phase. The valence-conduction inversion energy is 0.28 eV.

band ordering, and opens up a gap of 40 meV at the maximum strain, resulting in a TI phase. A representative band structure is shown in Fig. 1.

Topologically protected gapless surface states serve as direct confirmation of the topological bulk bands, and also serve directly as a bridge to experiment. The conducting character of these surface states is known to be robust against disorder, except when introduced by magnetic impurities (breaking TRS) [30]. As shown in Fig. 2, both (001) and (100) surfaces have surface states crossing the bulk gap of 30 meV. The (001) surface shows bands straightforwardly connecting the valence and conduction states, while the topological surface bands on the (100) surface incorporate a single Dirac point. These topological surface states are similar to those observed in Bi_2Te_3 , Sb_2Te_3 , and Bi_2Se_3 .

B. Uniaxial expansion

Expansion of the lattice parameter c of Ca_3BiP by 1–5% (the range we studied) also retains the band inverted ordering, but the different sign of eigenvalue splitting by SOC produces

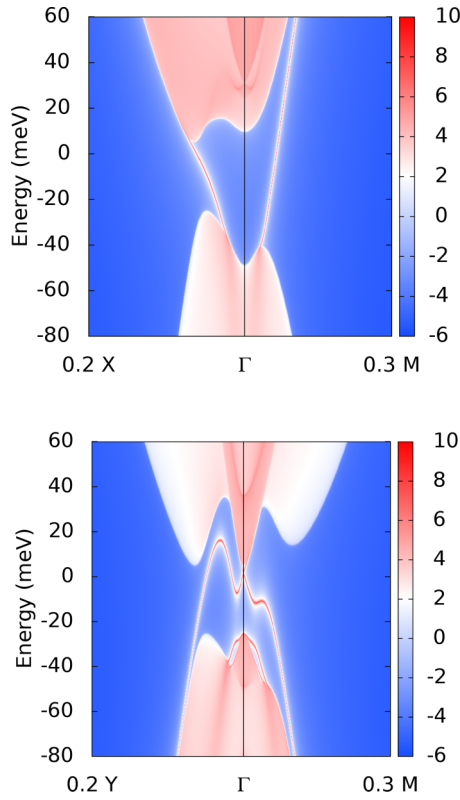


FIG. 2. Energy- and momentum-dependent spectral density of a semi-infinite crystal of (001)-compressed (5%) Ca_3BiP terminated on (001) (top panel) and (100) (bottom panel) surfaces. Redder colors represent higher intensity.

a different result. The surface spectrum displays a (twofold) linear band crossing along Γ -Z and gapped elsewhere as shown in Fig. 3. The band crossing point (fourfold degenerate including spins) is a signature of a quadruple Dirac point, and is unavoidable as the bands have different irreducible representations, i.e., Γ_6 and Γ_7 , as characterized and protected by the C_{4v} rotational point group symmetry.

The (100) surface shows topological surface bands crossing the projected bulk band gap of about 20 meV (Fig. 4). The Fermi surface exhibits two topologically nontrivial Fermi arcs touching at the Dirac nodes $\vec{k} = (0, 0, \pm k_c)$ protected by both

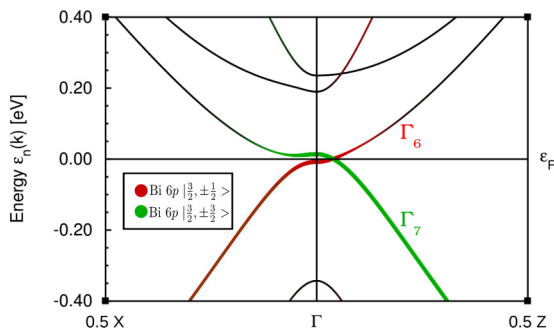


FIG. 3. Band structure of Ca_3BiP with tensile strain of 1% along (001) shows a Dirac point at $\vec{k} = (0, 0, k_c)$, where $k_c = 0.022 \text{ \AA}^{-1}$. Around k_c , the bands have Bi $6p \left| \frac{3}{2}, \pm \frac{1}{2} \right\rangle$ and $\left| \frac{3}{2}, \pm \frac{3}{2} \right\rangle$ characteristics.

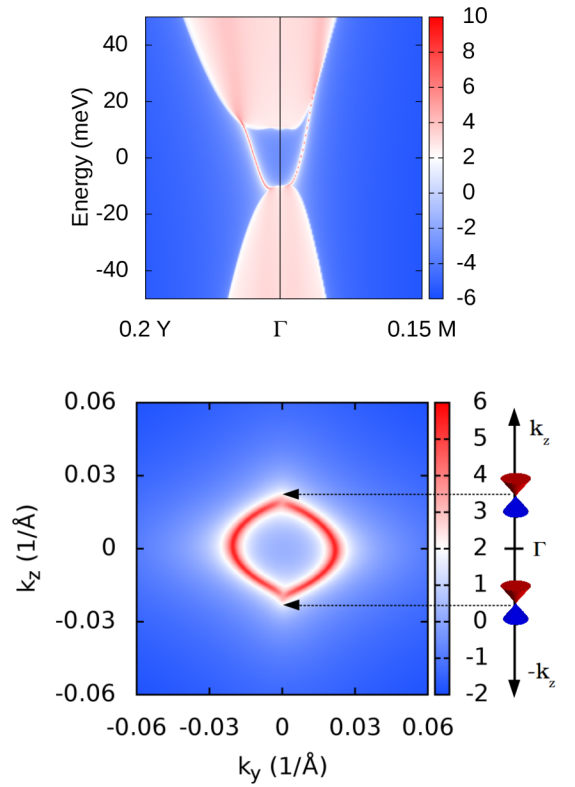


FIG. 4. Top panel: Energy- and momentum-dependent spectral density of a semi-infinite crystal of (001)-expanded Ca_3BiP terminated on the (100) surface. Bottom panel: The (100) surface shows two half-circle Fermi arcs connecting projections of Dirac points along $\pm k_z$.

IS and TRS. This single pair of Fermi arcs connecting two Dirac points, like the Fermi arc connecting Weyl points in a WSM, is possible to exist, as a Dirac point can be treated as two Weyl points with opposite chirality, which in this case do not annihilate each other since the degeneracy is protected by the crystal symmetry. One notable property of the Fermi arc is that, ideally, electron density on the Fermi arc of one surface can sink through the bulk to the Fermi arc of the opposite surface, while eigenvalues remain continuous.

C. Low energy description

An effective 4×4 Hamiltonian generalized from those used for Na_3Bi [31] and Cd_3As_2 [32] can be adopted to describe the Dirac band crossing at k_c in Fig. 3, with Bi $6p \left| \frac{3}{2}, \pm \frac{1}{2} \right\rangle$ and $\left| \frac{3}{2}, \pm \frac{3}{2} \right\rangle$ states as the basis, in the order of $J_z = \frac{1}{2}, -\frac{3}{2}, -\frac{1}{2}, \frac{3}{2}$, after SOC. The Hamiltonian for the C_4 symmetry of Ca_3BiP around Γ reads, after (001) strain,

$$H_{\Gamma}(k) = \varepsilon_0(k) + \begin{pmatrix} M(k) & Ak_+ & 0 & 0 \\ Ak_- & -M(k) & 0 & 0 \\ 0 & 0 & M(k) & -Ak_- \\ 0 & 0 & -Ak_+ & -M(k) \end{pmatrix}, \quad (1)$$

where the bands are $M(k) = M_0 - M_1 k_z^2 - M_2(k_x^2 + k_y^2)$ with negative constants to reproduce band inversion, $k_{\pm} = k_x \pm ik_y$, and A provides the scale for coupling to uniaxial strain along \hat{z} . $k_c = \sqrt{M_0/M_1}$ gives the band crossing

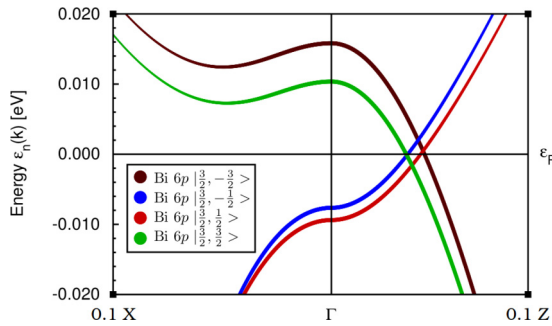


FIG. 5. Weyl nodes at $\vec{k}_0^* = (0, 0, k_0^*)$ under an external magnetic field of $B = 24$ T. The bands are mostly split along k_z and minimally in energy.

point along \hat{z} , and the dispersion around k_0 yields $E_{k_0} = \pm\sqrt{[2k_0\delta k_z - M_2(\delta k_x^2 + \delta k_y^2)]^2 + A^2(\delta k_x^2 + \delta k_y^2)}$.

Time reversal symmetry breaking. The Hamiltonian in Eq. (1) remains block-diagonal, containing two multi-Weyl Hamiltonian systems of opposite chirality. Symmetry can be broken further by violating IS or TR symmetry. Breaking IS is not an easy route, since the fourfold symmetry of Eq. (1) is to be preserved, otherwise it will open a gap and generate massive fermions. A simpler means is to apply an external Zeeman magnetic field B coupling to the SOC basis sets, which preserves the crystal symmetry but breaks TRS [33]:

$$H_{\text{Zeeman}}(k) = H_{\Gamma}(k) + \begin{pmatrix} \Delta p_1 & 0 \\ 0 & \Delta p_2 \end{pmatrix} \otimes \sigma_z \quad (2)$$

where $\Delta p_{1,2} = \frac{1}{2}g_{1,2}\mu_0 B$ for Bi $6p_{3/2, \pm 1/2}$ and $6p_{1/2, \pm 1/2}$ states respectively. Equation (2) can be block-diagonalized into 2×2 matrices,

$$H_{\pm}(k) = \left[M(k) \pm \frac{(\Delta p_1 - \Delta p_2)}{2} \right] \sigma_z \pm \left[\frac{(\Delta p_1 + \Delta p_2)}{2} \right] I \pm A(k_x \sigma_x + k_y \sigma_y). \quad (3)$$

The Weyl nodes are displaced to $\vec{k}_0^* = (0, 0, k_0^*)$, where $k_0^* = \sqrt{\frac{M_0}{M_1} \pm \frac{\Delta p_1 - \Delta p_2}{2M_1}}$. Expansion around \vec{k}_0^* gives $E_{k_0^*} = \pm\sqrt{[2k_0^*\delta k_z - M_2(\delta k_x^2 + \delta k_y^2)]^2 + A^2(\delta k_x^2 + \delta k_y^2)} \pm (\Delta p_1 + \Delta p_2)/2$, where the Weyl Hamiltonians are decoupled along \hat{z} into k_0^* and shifted in energy by the average of the magnetic energies.

Figure 5 illustrates the final spectrum for $B = 24$ T ($\mu_B B \approx 1$ meV), for which the degeneracies are located at $k_{z,j} = \pm 0.020 \text{ \AA}^{-1}$, $\pm 0.022 \text{ \AA}^{-1}$, $\pm 0.023 \text{ \AA}^{-1}$, and $\pm 0.024 \text{ \AA}^{-1}$. The first and last lie at E_F and occur for bands of opposite sign in J_z , while the middle two are for equal sign in J_z and occur above and below E_F . We observe that the nodes lying at E_F are *multi-Weyl points*: they have linear dispersion along k_z , as shown in Fig. 5, and are quadratic in the k_x, k_y plane. A quantitative description in a tight binding scheme

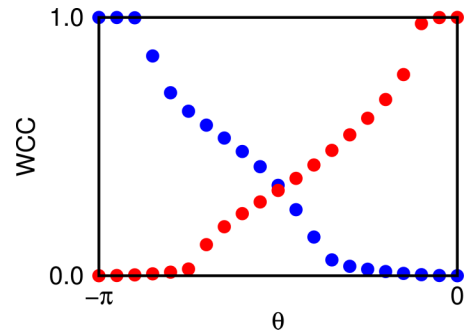


FIG. 6. The Wannier charge center (WCC) is computed for each loop at a constant azimuthal angle θ around a sphere surrounding Weyl points at $k_z = 0.020 \text{ \AA}^{-1}$ (blue) and 0.024 \AA^{-1} (red). The change in the charge polarization for each loop from south ($\theta = -\pi$) to north ($\theta = 0$) for blue and red curves indicates -1 and $+1$ chiralities, respectively.

derived from maximally localized Wannier functions [26] is provided in the Supplemental Material [34]. Our calculation of Na_3Bi shows similar behavior.

The flow of the hybrid Wannier charge center (WCC) provides direct confirmation of the topological character. By constructing a closed 2D cut of the Brillouin zone containing a Weyl node, the evolution of the band sum of the hybrid WCCs around the closed cut can be calculated to determine the Weyl chirality [35]. Figure 6 shows the evolution of the charge polarization of the two Weyl nodes at E_F , which indicates their corresponding chiralities $C_w = (-1, +1)$.

IV. SUMMARY

In summary, we have shown that members of this class of APv materials can be driven into various topological phases by symmetry breaking. SOC, strain, and magnetic field can drive a cascade through a variety of topological phases. SOC drives or deepens band inversion by splitting the $Pn p_{3/2}$ eigenvalues upward beyond the s conduction band at Γ , leaving a topological band-touching semimetal. Uniaxial strain breaks the degeneracy and, if compressive, produces a topological insulator, while, if tensile, gives a Dirac semimetal. At that point, application of a magnetic field breaks TRS and splits each Dirac node into a pair of Weyl nodes with opposite chirality, yielding a multi-Weyl points whose bounding projections are joined by Fermi arcs.

ACKNOWLEDGMENTS

We acknowledge fruitful interactions with K.-W. Lee and A. M. Essin. This work was supported by the NSF DMREF program under Grant DMR-1534719. The calculations used resources of the National Energy Research Scientific Computing Center (NERSC), a DOE Office of Science User Facility supported by the Office of Science of the U.S. Department of Energy under Contract No. DE-AC02-05CH11231.

[1] M. Z. Hasan and C. L. Kane, Colloquium: Topological insulators, *Rev. Mod. Phys.* **82**, 3045 (2010).

[2] X. Wan, A. M. Turner, A. Vishwanath, and S. Y. Savrasov, Topological semimetal and Fermi-arc surface states in the

- electronic structure of pyrochlore iridates, *Phys. Rev. B* **83**, 205101 (2011).
- [3] C. Fang, M. J. Gilbert, X. Dai, and B. A. Bernevig, Multi-Weyl Topological Semimetals Stabilized by Point Group Symmetry, *Phys. Rev. Lett.* **108**, 266802 (2012).
- [4] V. Pardo and W. E. Pickett, Half-Metallic Semi-Dirac-Point Generated by Quantum Confinement in TiO_2/VO_2 Nanostructures, *Phys. Rev. Lett.* **102**, 166803 (2009).
- [5] S. Banerjee, R. R. P. Singh, V. Pardo, and W. E. Pickett, Tight-Binding Modeling and Low Energy Behavior of the Semi-Dirac Point, *Phys. Rev. Lett.* **103**, 016402 (2009).
- [6] H. Huang, Z. Liu, H. Zhang, W. Duan, and D. Vanderbilt, Emergence of a Chern-insulating state from a semi-Dirac dispersion, *Phys. Rev. B* **92**, 161115(R) (2015).
- [7] D. Hsieh, D. Qian, L. Wray, Y. Xia, Y. S. Hor, R. J. Cava, and M. Z. Hasan, A topological Dirac insulator in a quantum spin hall phase, *Nature (London)* **452**, 970 (2008).
- [8] H. Zhang, C. X. Liu, X. L. Qi, X. Dai, Z. Fang, and S. C. Zhang, Topological insulators in Bi_2Se_3 , Bi_2Te_3 and Sb_2Te_3 with a single Dirac cone on the surface, *Nat. Phys.* **5**, 438 (2009).
- [9] W. Zhang, R. Yu, H. J. Zhang, X. Dai, and Z. Fang, First-principles studies of the three-dimensional strong topological insulators Bi_2Te_3 , Bi_2Se_3 and Sb_2Te_3 , *New J. Phys.* **12**, 065013 (2010).
- [10] O. V. Yazyev, J. E. Moore, and S. G. Louie, Spin Polarization and Transport of Surface States in the Topological Insulators Bi_2Se_3 and Bi_2Te_3 from First Principles, *Phys. Rev. Lett.* **105**, 266806 (2010).
- [11] R. Li, Q. Xie, X. Cheng, D. Li, Y. Li, and X. Q. Chen, First-principles study of the large-gap three-dimensional topological insulators $M_3\text{Bi}_2$ ($M = \text{Ca}, \text{Sr}, \text{Ba}$), *Phys. Rev. B* **92**, 205130 (2015).
- [12] Y. Ando, Topological insulator materials, *J. Phys. Soc. Jpn.* **82**, 102001 (2013).
- [13] J. Li *et al.*, Two-dimensional topological insulators with tunable band gaps: Single-layer HgTe and HgSe, *Sci. Rep.* **5**, 14115 (2015).
- [14] H. Jin, J. Im, and A. J. Freeman, Topological insulator phase in halide perovskite structures, *Phys. Rev. B* **86**, 121102 (2012).
- [15] H. Weng, X. Dai and Z. Fang, Topological semimetals predicted from first-principles calculations, *J. Phys.: Condens. Matter* **28**, 303001 (2016).
- [16] R. Yu, H. Weng, Z. Fang, X. Dai, and X. Hu, Topological Node-Line Semimetal and Dirac Semimetal State in Antiperovskite Cu_3PdN , *Phys. Rev. Lett.* **115**, 036807 (2015).
- [17] S. Xu *et al.*, Discovery of a Weyl Fermion semimetal and topological Fermi arcs, *Science* **349**, 613 (2015).
- [18] G. Xu, H. M. Weng, Z. J. Wang, X. Dai, and Z. Fang, Chern Semimetal and the Quantized Anomalous Hall Effect in HgCr_2Se_4 , *Phys. Rev. Lett.* **107**, 186806 (2011).
- [19] Y. Quan and W. E. Pickett, Single Nodal Loop of Accidental Degeneracies in Minimal Symmetry Triclinic CaAs_3 , *Phys. Rev. Lett.* **118**, 176402 (2017).
- [20] Y. Sun, X. Q. Chen, S. Yunoki, D. Li, and Y. Li, New Family of Three-Dimensional Topological Insulators with Antiperovskite Structure, *Phys. Rev. Lett.* **105**, 216406 (2010).
- [21] W. F. Goh and W. E. Pickett, Survey of the class of isovalent antiperovskite alkaline-earth pnictide compounds, *Phys. Rev. B* **97**, 035202 (2018).
- [22] R. Niewa, Alkaline-earth metal nitrides of the main-group elements: Crystal structures and properties of inverse perovskites, *Z. Anorg. Allg. Chem.* **639**, 1699 (2013).
- [23] K. Koepnick and H. Eschrig, Full-potential nonorthogonal local-orbital minimum-basis band-structure scheme, *Phys. Rev. B* **59**, 1743 (1999).
- [24] J. P. Perdew, K. Burke, and M. Ernzerhof, Generalized Gradient Approximation Made Simple, *Phys. Rev. Lett.* **77**, 3865 (1996).
- [25] L. Fu and C. L. Kane, Topological insulators with inversion symmetry, *Phys. Rev. B* **76**, 045302 (2007).
- [26] N. Marzari, A. A. Mostofi, J. R. Yates, I. Souza, and D. Vanderbilt, Maximally localized Wannier functions: Theory and applications, *Rev. Mod. Phys.* **84**, 1419 (2012).
- [27] P. Blaha, K. Schwarz, G. Madsen, D. Kvasnicka, and J. Luitz, *WIEN2K: An Augmented Plane Wave + Local Orbitals Program for Calculating Crystal Properties* (Technische Universität Wien, Vienna, 2001).
- [28] M. P. Lopez Sancho, J. M. Lopez Sancho, J. M. L. Sancho and J. Rubio, Highly convergent schemes for the calculation of bulk and surface Green functions, *J. Phys. F* **15**, 851 (1985).
- [29] Q. Wu, S. Zhang, H. F. Song, M. Troyer, and A. A. Soluyanov, WannierTools: An open-source software package for novel topological materials, *Comput. Phys. Commun.* **224**, 405 (2017).
- [30] Y. L. Chen, J. H. Chu, J. G. Analytis, Z. K. Liu, K. Igarashi, H. H. Kuo, X. L. Qi, S. K. Mo, R. G. Moore, D. H. Lu, M. Hashimoto, T. Sasagawa, S. C. Zhang, I. R. Fisher, Z. Hussain and Z. X. Shen, Massive Dirac fermion on the surface of a magnetically doped topological insulator, *Science* **329**, 659 (2010).
- [31] Z. Wang, Y. Sun, X. Q. Chen, C. Franchini, G. Xu, H. Weng, X. Dai and Z. Fang, Dirac semimetal and topological phase transitions in $A_3\text{Bi}$ ($A = \text{Na}, \text{K}, \text{Rb}$), *Phys. Rev. B* **85**, 195320 (2012).
- [32] Z. Wang, H. Weng, Q. Wu, X. Dai and Z. Fang, Three-dimensional Dirac semimetal and quantum transport in Cd_3As_2 , *Phys. Rev. B* **88**, 125427 (2013).
- [33] H. Z. Lu and S. Q. Shen, Quantum transport in topological semimetals under magnetic fields, *Front. Phys.* **12**, 127201 (2017).
- [34] See Supplemental Material at <http://link.aps.org/supplemental/10.1103/PhysRevB.98.125147> for plots showing the dispersion perpendicular to the Γ -Z line that verifies the Dirac or semi-Weyl dispersion of each of the four crossings shown in Fig. 5.
- [35] D. Gresch, G. Autès, O. V. Yazyev, M. Troyer, D. Vanderbilt, B. A. Bernevig, and A. A. Soluyanov, $Z_2\text{Pack}$: Numerical implementation of hybrid Wannier centers for identifying topological materials, *Phys. Rev. B* **95**, 075146 (2017).